



ELSEVIER

Physica D 110 (1997) 105–122

PHYSICA D

Quantifying transport in numerically generated velocity fields

P.D. Miller^{a,*}, C.K.R.T. Jones^a, A.M. Rogerson^b, L.J. Pratt^b

^a *Division of Applied Mathematics, Brown University, Providence, RI 02912, USA*

^b *Woods Hole Oceanographic Institution, Woods Hole, MA 02543, USA*

Received 11 September 1996; received in revised form 30 April 1997; accepted 7 May 1997

Communicated by J.D. Meiss

Abstract

Geometric methods from dynamical systems are used to study Lagrangian transport in numerically generated, time-dependent, two-dimensional (2D) vector fields. The flows analyzed here are numerical solutions to the barotropic, β -plane, potential vorticity equation with viscosity, where the partial differential equation (PDE) parameters have been chosen so that the solution evolves to a meandering jet. Numerical methods for approximating invariant manifolds of hyperbolic fixed points for maps are successfully applied to the aperiodic vector field where regions of strong hyperbolicity persist for long times relative to the dominant time period in the flow. Cross sections of these 2D “stable” and “unstable” manifolds show the characteristic transverse intersections identified with chaotic transport in 2D maps, with the lobe geometry approximately recurring on a time scale equal to the dominant time period in the vector field. The resulting lobe structures provide time-dependent estimates for the transport between different flow regimes. Additional numerical experiments show that the computation of such lobe geometries are very robust relative to variations in interpolation, integration and differentiation schemes.

1. Introduction

Recently, there has been much interest in applying methods from dynamical systems to the study of transport and mixing in fluids. For time-periodic 2D flows the transport dynamics can be reduced to the study of the associated Poincaré map on \mathbb{R}^2 . In such flows the mechanism for chaotic transport is the existence of hyperbolic fixed points for the map and the transverse intersection of their associated invariant manifolds. Segments of the invariant manifolds are used to partition the phase space into regions with distinctly

different motions and transport of fluid from one flow regime to another is understood via the dynamics of the lobes resulting from the intersecting manifolds. The theory of lobe dynamics is well established as a technique for characterizing and quantifying transport in time-periodic 2D flows [8,17,19,24,25,28] and has been extended to flows with quasiperiodic time dependence [4,10,28].

The motivation behind the work presented here is to apply techniques in dynamical systems analysis to the study of transport for idealized dynamical models of oceanic flows where the time-dependent vector fields are generated as the numerical solution to an appropriate governing system of partial differential equations (PDEs). For these numerically generated, incompressible, 2D flow fields the velocity vector

* Corresponding author.

(or streamfunction) is prescribed only at discrete spatial and temporal points, on some finite interval of time. The velocity field to be analyzed contains the full dynamics of the governing dynamical equations as opposed to analyzing a system of ordinary differential equations (ODEs) derived under certain simplifying assumptions (for example, modal truncation in the PDE or linearization of the dynamical equations about some base flow). Invariant manifold techniques appropriate to time-periodic vector fields have been applied to numerical simulations of the governing equations in cases where the initial conditions evolve asymptotically to a time-periodic solution [3,11,27]. However, generically we expect the time dependence of numerically generated velocity fields to be neither periodic nor quasiperiodic, requiring that the PDE solutions be tracked for much longer time intervals and that methods be developed for characterizing transport in aperiodic flows.

Motivated by Lagrangian observations of the Gulf Stream [6], there has been much interest in understanding the mixing and fluid exchange associated with meandering jets. The flow analyzed here is a numerical model of a meandering jet, where the governing equation is the barotropic, β -plane, potential vorticity equation with viscosity. The purpose for studying this particular model is to evaluate the effect of viscosity on transport and mixing in a flow simulating a meandering jet with relatively simple time dependence and where the full nonlinearity has been accounted for in the velocity field (see the related work by Rogerson et al. [22]). Using vector fields which satisfy the full nonlinear dynamical equations is an improvement over earlier models in which the vector fields are either purely kinematic [5,10,12,26], or constructed from the superposition of linear neutral modes [9,18,20]. The viscosity is required for numerical stability as well as being motivated by recent work regarding the relationship of potential vorticity conservation and chaotic transport in incompressible, 2D flows [2,7].

With the vector fields prescribed only at discrete spatial and temporal grid points and the data base being quite large in many cases, just integrating individual particle trajectories requires considerable

numerical machinery. Moreover, one would hope that the methods for reconstructing the Lagrangian particle paths are efficient enough that it is feasible to investigate the flow interactively with a dynamical systems package such as *DsTool*. In this respect, it is expected that the identification of geometric structures such as invariant manifolds and their associated lobes will not depend strongly on the particular numerical schemes used in reconstructing trajectories. Results of numerical experiments are discussed in Section 8 verifying that these geometric structures are indeed robust with respect to variations in the numerical schemes. On the other hand, small changes in the numerics can have a significant effect on individual trajectories, particularly for fluid particles passing near regions of strong hyperbolicity.

The meandering jets investigated here are close to being periodic in time when viewed in a reference frame moving along with the propagating meander and, as a first approach to quantifying the fluxes between different flow regimes, the dominant time dependency in the moving frame is used to define a time-periodic flow which approximates the aperiodic flow. The Poincaré map for this periodic flow defined from the truncated data set has hyperbolic fixed points and transversely intersecting invariant manifolds, and the lobe dynamics are analyzed in the usual way. In Section 5, the techniques used to identify these hyperbolic fixed points and their invariant manifolds are detailed and transport estimates presented.

The main goal of the work presented here is to develop techniques for characterizing and quantifying transport in flows having more general time dependencies and, to this end, these flows for meandering jets serve well as a first step away from time-periodic flows. All of the simulations have regions of strong hyperbolicity which remain well-separated from one another and nearly stationary in the reference frame moving with the meander. Moreover, these hyperbolic regions exist for times much longer than the period used in the periodic approximation and it is possible to generate lobe structures very similar to the lobes computed for the Poincaré map. Though the partitioning of the phase space into different flow regimes is

no longer fixed for all time, we expect that there is still a clearly defined exchange of fluid between different flow regimes via the mechanism of intersecting manifolds and lobe dynamics, with the transport no longer independent of time. It is important to note that an advantage to working with a periodic flow is that the manifolds can be iterated to any length making it possible to follow several iterations of a lobe, using only a fixed amount of data. However, for the aperiodic data, tracking the lobes over several iterations is limited by the available length of the data set.

The rest of the paper is organized as follows. Section 2 presents the numerical model used to simulate a meandering barotropic jet and describes the time dependency of the solution sets. Section 3 is a discussion of the numerical methods used to reconstruct Lagrangian trajectories from these numerical databases. Section 4 introduces the method of lobe dynamics and the characterization of transport within time-periodic, 2D flows. In Section 5 we describe our approach for estimating the fluxes in a time-periodic flow which approximates the aperiodic flow field. The main result of the paper is in Section 6 where the analysis of lobe dynamics is successfully applied to the fully aperiodic vector field, with some discussion of these results to follow in Section 8.

2. Model for a meandering barotropic jet

A meandering jet flow is simulated numerically using the model of Flierl et al. [13]. The governing PDE is the nondimensional barotropic potential vorticity equation with a viscosity term added,

$$\frac{Dq}{Dt} = (Re)^{-1} \nabla^2 q. \quad (1)$$

Using $\psi(x, y, t)$ to denote the streamfunction for the incompressible 2D flow, the barotropic potential vorticity is given by $q = \nabla^2 \psi + \beta y$, where β is the linear variation in the planetary vorticity as determined by the latitude of the jet. Instead of the superviscosity used in [13], this formulation uses a Newtonian viscosity term as described in [22]. Rewriting the PDE in terms of the streamfunction,

$$\frac{\partial}{\partial t} \nabla^2 \psi + J(\psi, \nabla^2 \psi) + \beta \frac{\partial \psi}{\partial x} = (Re)^{-1} \nabla^4 \psi. \quad (2)$$

Here ∇^2 denotes the Laplacian, $J(f, g) = f_x g_y - f_y g_x$ is the Jacobian of (f, g) , and the inverse of the Reynold's number $(Re)^{-1}$ characterizes the strength of an eddy-type viscosity.

The PDE is in two spatial dimensions with x denoting the eastward direction and y pointing to the north. The equation in (2) was solved numerically in a square domain of dimension $L_x = L_y = 25.6$ with doubly periodic boundary conditions, using a pseudo-spectral code with both 64×64 Fourier modes and 128×128 modes. The initial data for ψ is a weak perturbation of an unstable zonal jet,

$$\begin{aligned} \psi(x, y, 0) = & -\operatorname{erf}(y) + 2y/L_y \\ & + \delta \exp(-y^2) \sin(k_0 x). \end{aligned}$$

The wave number k_0 is constrained by the periodicity, $k_0 = 2\pi n_0/L_x$, for some positive integer n_0 and the body of the jet flows in the eastward direction, centered at $y = 0$. The work of [13] identified parameter values of β and n_0 such that the unstable initial flow evolves into a jet with large-amplitude and nearly steadily propagating meanders. Fig. 1 shows snapshots of the potential vorticity contours as the PDE solution evolves from its initial state into a nearly steady meandering jet, for parameter values $(Re, \beta, n_0) = (10^4, 0.207, 4)$. In a reference frame moving with the meander there are three distinct regions to the flow: the meandering “jet core” or “prograde” region where the flow is eastward, the “recirculation” or “vortex” regions lying to the north and south of the jet in between meanders, and the far field where the flow is westward or “retrograde”.

The PDE in (1) implies that potential vorticity is nearly conserved when the Reynold's number is large and therefore, the potential vorticity contours give some indication of the dynamics of the Lagrangian transport within the evolving flow. When viewed in a stationary frame the data for the meandering jet simulation has a dominant time dependency associated with the propagation speed and spatial frequency of the meander. Having identified the dominant time period T_0 , the propagation speed of the meander is determined

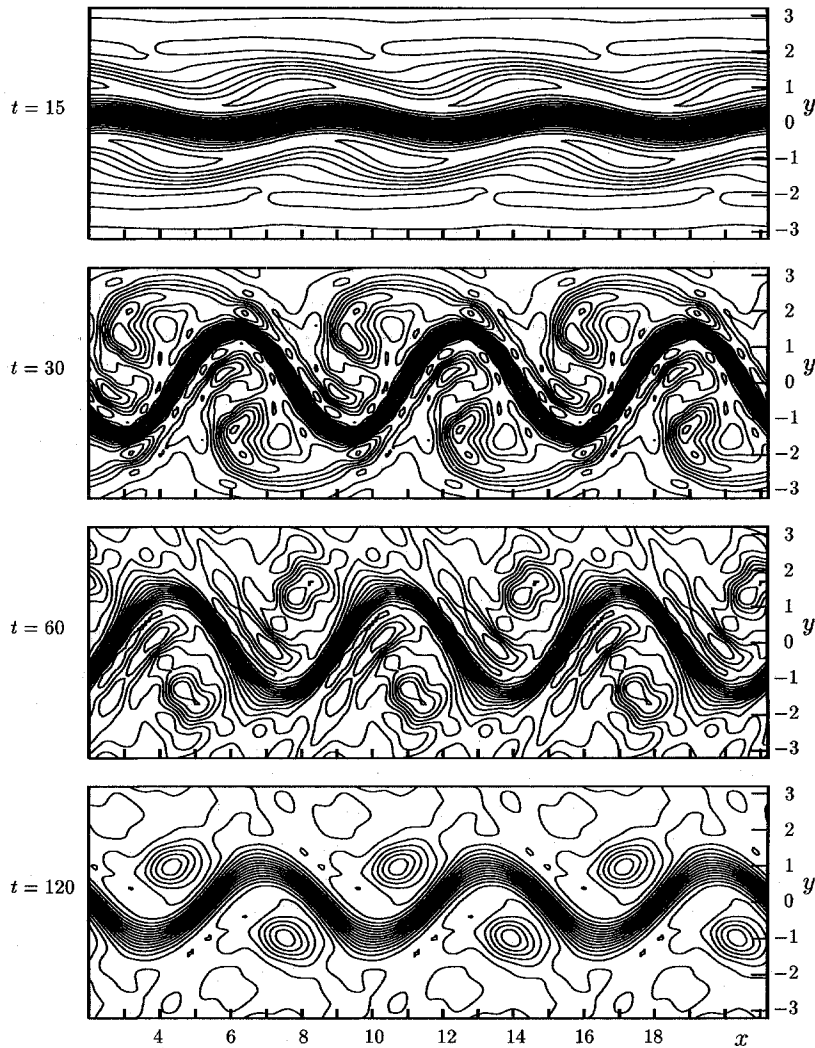


Fig. 1. Level sets of potential vorticity showing the evolution of the PDE solution into a jet with large-amplitude meanders propagating with speed c . The solution has been computed on a 64×64 spatial grid covering the domain $0 \leq x \leq 25.6$ and $-12.8 \leq y \leq 12.8$. The parameter values for the simulation shown here are $(Re, \beta, n_0) = (10^4, 0.207, 4)$. The potential vorticity contours are incremented in steps of 0.10.

by $c = L_x/(n_0 T_0)$. Though the flows are not strictly quasiperiodic in time, there is an approximately recurrent behavior to the vector field when viewed in a reference frame moving with the meander. This recurrence, with time period T_1 , is observed as an oscillation in the meander amplitude and a rotation of the potential vorticity contours within the vortex regions of the flow. An example of this is shown in Fig. 2 for the case $(Re, \beta, n_0) = (10^4, 0.207, 4)$.

In all the data sets investigated it is clear from the evolution of the potential vorticity contours that the largest exchange of fluid is taking place between the vortex region and the retrograde region, while the strong potential vorticity gradients near the axis of the jet act as barriers to transport. However, more than just observing where the transport is taking place, our goal is to quantify the volume of fluid being exchanged between different regions of the flow using techniques

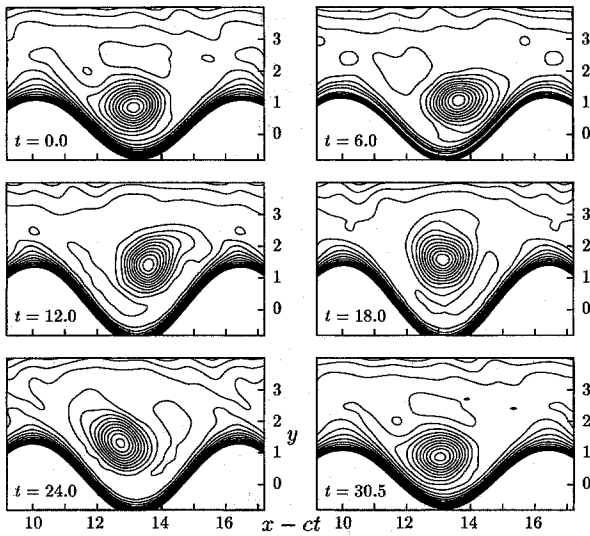


Fig. 2. Detail of potential vorticity contours in the vortex region as viewed in the moving reference frame for $(Re, \beta, n_0) = (10^4, 0.207, 4)$, computed on a 64×64 grid. These snapshots cover one time period T_1 as used in defining the time-periodic flow. Note that the potential vorticity is more homogeneous than in Fig. 1 and the contours are now incremented in steps of 0.05.

from dynamical systems. As described in Section 4, the method of lobe dynamics is well established as a tool for studying transport in time-periodic 2D flows, where the fluxes are characterized via the transverse intersection of stable and unstable manifolds associated with saddle-type fixed points of the Poincaré map. The area of the lobes resulting from these transverse intersections averaged over the time period of the map determines the flux across the particular boundary.

As a first approach to estimating the transport, the lobe dynamics are computed for a periodic flow which approximates the aperiodic flow in the moving reference frame. The period of this truncated flow is just the dominant time period of the velocity field in the moving reference frame, T_1 . The details of this approach are described in Section 5 where the results are presented for the case $(Re, \beta, n_0) = (10^4, 0.207, 4)$ computed on a 64×64 spatial grid. A more complete dynamical systems analysis for the periodic flows is included in [22] where results are presented on four different data sets, $(Re, \beta, n_0) = (10^4, 0.103, 3)$, $(10^3, 0.103, 3)$, $(10^4, 0.207, 4)$, and $(10^3, 0.207, 4)$,

computed on the finer spatial grid, $\Delta x = \Delta y = 0.2$, using 128×128 spatial Fourier modes. The emphasis in this paper is on applying similar methods to the full aperiodic data set as presented in Section 6.

3. Reconstructing Lagrangian trajectories

In this section we discuss the methods used in reconstructing Lagrangian trajectories from the PDE solution described in Section 2. Consider a 2D flow where $u(x, y, t)$ and $v(x, y, t)$ are the components of the velocity field as determined from a governing system of PDEs. Lagrangian trajectories of fluid parcels satisfy the system of ordinary differential equations,

$$\frac{dx}{dt} = u(x, y, t), \quad \frac{dy}{dt} = v(x, y, t). \quad (3)$$

For incompressible 2D flows the velocity components may be given as derivatives of a scalar streamfunction $\psi(x, y, t)$ with $u = -\psi_y$ and $v = \psi_x$. We wish to solve the system in (3) when the vector field is known only at discrete spatial and temporal grid points as a numerical solution to the PDE. We refer to this database for the vector field of the ODE as a *numerically generated velocity field*.

The spatial domain is assumed rectangular with dimension $L_x \times L_y$. The discretized mesh is uniform with grid spacings Δx and Δy , and the spatial grid points denoted by (x_j, y_k) , for $0 \leq j \leq J$ and $0 \leq k \leq K$. Here x_0, y_0 denote the lower boundaries and x_J and y_K the upper boundaries. With this notation, the spatial dimensions satisfy $L_x = J \cdot \Delta x$ and $L_y = K \cdot \Delta y$. In the numerical simulation of the meandering jet discussed in Section 2, the computational domain is doubly periodic with $x_J = x_0$ and $y_K = y_0$.

The database consists of N slices of data where the n th slice is the computed PDE solution at time $t_n = t_0 + n \cdot \Delta t$, for $n = 0, 1, \dots, N - 1$. Each data slice is a 2D array of data defining the velocity field (or streamfunction) on the $(J + 1) \times (K + 1)$ spatial grid points, at a fixed time t_n . For vector fields periodic in time with period $T = N \cdot \Delta t$, the slice at $t = t_N$ is identical to the slice at $t = t_0$. The time t_0 represents the first time in the PDE at which the solution is written

to the database. Here t_0 is chosen to be some time at which the flow has settled into a statistically steady configuration.

3.1. Integrating the numerical vector field

Integrating the ODEs for a numerically generated vector field requires interpolation in the full 3D space to find the velocity field at arbitrary points (x, y, t) . We treat the 1D interpolation in time separately from the 2D interpolation in x - y space. The temporal interpolation is determined by the stepsize Δt of the data set and the choice of stepsize in the ODE solver, both of which we have control over. All the results presented here are computed using the fourth-order Runge–Kutta method to integrate the vector field. To solve (3) without using any temporal interpolation, the Runge–Kutta uses an integration stepsize of $h = 2 \cdot \Delta t$, and any interpolation in time should necessarily be a local interpolation since nonlocal methods will be very inefficient.

The most accurate reproduction of Lagrangian trajectories will occur if the PDE solution is output at every time slice available from the PDE solver. In practice this may lead to prohibitively large data files and we expect to analyze the PDE data at a coarser timestep depending on the time scales present in the solution. For the dynamical systems analysis presented in Section 6 numerical experiments indicate that the results are not affected significantly by using a data base with a coarser timestep, but rather, with regard to the lobe analysis, it is more valuable to have the data set cover a larger interval of time. Using interpolation to integrate the coarser data set at a smaller stepsize h is shown to have even less effect on the results. Observations from these numerical experiments are discussed in Section 8.

This process of computing particle trajectories from a numerically generated vector field has been integrated into *DsTool*, the dynamical systems package developed at Cornell, enabling us to interactively view the dynamics of these flows. However, many of the fixed point and invariant manifold computations could not be performed adequately from within this package and had to be computed using code designed specif-

ically for handling the numerical database in a more efficient manner.

3.2. Interpolation in x - y space

The usual approach to interpolating in the 2D phase space is to use local polynomial approximations, typically of sixth-order (see [1]). Local polynomials give good accuracy and are computationally efficient, requiring just the value of the scalar function at a number of nearby grid points. For example, the sixth-order method uses a fifth-order polynomial in x and y to fit the scalar function at the nearest 36 nodes. The interpolation is performed independently for each of the velocity components with the resulting field continuous in x and y , though the interpolated functions will not have continuous derivatives. This lack of smoothness in the local polynomial interpolation serves to break the Hamiltonian structure of incompressible 2D flows. For incompressible flows the velocity vector (u, v) is defined at each of the grid points (x_j, y_k, t_n) as the spatial derivatives of a streamfunction $\psi(x_j, y_k, t_n)$. The interpolations for ψ , u , and v are done independently of one another, and although each of these functions is continuous, the relationships $u = -\psi_y$ and $v = \psi_x$ will not be satisfied at arbitrary points (x, y, t_n) . The flow as determined by polynomial interpolation is no longer area preserving. To maintain the Hamiltonian structure in the system of ODEs it is necessary to interpolate the streamfunction with a scheme that provides smoothness through at least the first derivatives. We have considered three approaches which provide additional smoothness: a (local) bicubic interpolation, trigonometric interpolation, and bicubic splines.

Bicubic interpolation is a local method requiring values of ψ , ψ_x , ψ_y and ψ_{xy} at the four nearest grid points. The interpolation uses a third-order polynomial to fit the scalar function ψ and its three derivatives at the four surrounding nodes (see [21]). Since we are only provided with the streamfunction, the first and second derivatives must be approximated using ψ evaluated at the grid points. Numerical differencing is the quickest way to estimate the derivatives, or if Fourier coefficients are readily available,

the derivatives can be determined to spectral accuracy by a simple multiplication in the frequency domain.

All orders of smoothness can be obtained by using a 2D trigonometric interpolation, where the Fourier coefficients of the streamfunction are denoted by $\hat{\psi}(\omega_m^x, \omega_n^y, t_k)$,

$$\psi(x, y, t_k) = \sum_j \sum_k \hat{\psi}(\omega_j^x, \omega_k^y, t_n) e^{-i\omega_j^x x} e^{-i\omega_k^y y}. \quad (4)$$

This method provides full spectral accuracy and is as smooth as we need but computationally costly unless a large number of spatial modes can be removed with little effect on the results. When the spatial domain is periodic, spectral interpolation can provide a benchmark for comparing other interpolation schemes.

Bicubic splines also provide the necessary global smoothness and only require evaluations of the scalar function. However, this is a nonlocal method always incorporating knowledge of the function over the entire spatial domain. One motivation is to keep the process as efficient as possible to facilitate interactive viewing of the dynamics. For this reason the preference is to work as much as possible with local numerical schemes. Some numerical observations discussed in Section 8 indicate that the lobe analysis in Sections 5 and 6 does not depend significantly on variations in interpolation schemes.

For much of the analysis presented here, local bicubic interpolation is used to compute the vector field during the integration of the ODEs. As discussed in Section 2, the spatial domain is doubly periodic and the PDE solver uses a pseudo-spectral code. The necessary derivatives are precomputed using the spectral representation of the streamfunction. The resulting derivatives are transformed back to x - y space and local bicubic interpolation is used to compute the vector field during the integration of the vector field. This extensive use of fast Fourier transforms is not very efficient but is required only when loading a new block of data slices into active memory. This approach is a compromise between accuracy and computational efficiency. We retain the Hamiltonian structure of the 2D flow with full spectral accuracy at

the points, as well as gaining some of the efficiency of a local interpolation scheme.

4. Chaotic transport in time-periodic 2D flows

Transport in the numerical simulation of the jet will first be estimated using a truncated data set which serves as a periodic approximation to the aperiodic data set. As way of background, we present a brief description of chaotic transport via lobe dynamics for time-periodic 2D flows where the Lagrangian trajectories of the fluid parcels are governed by the system of ODEs in (3). If the flow is incompressible, there exists a scalar streamfunction $\psi(x, y, t)$ which determines the velocity components by $u = -\psi_y$ and $v = \psi_x$. In the case where $u(x, y, t)$ and $v(x, y, t)$ are periodic in t with period T , we use the periodicity of the vector field to define the Poincaré map (or *first return map*) relative to time t_0 ,

$$\mathcal{P} : \mathbb{R}^2 \rightarrow \mathbb{R}^2, \quad \mathcal{P}(\mathbf{x}_0) = \phi(t_0 + T; \mathbf{x}_0, t_0), \quad (5)$$

where $\mathbf{x}(t) = \phi(t; \mathbf{x}_0, t_0)$ denotes the solution to (3) satisfying $\mathbf{x}(t_0) = \mathbf{x}_0$.

For time-periodic flows much of the phase-space transport can be understood by studying the dynamics of the associated Poincaré map. The key structures we wish to study are hyperbolic fixed points and their associated invariant manifolds. Transverse intersections of stable and unstable manifolds imply the presence of chaotic dynamics and the transport of fluid between regions of phase space having qualitatively different behavior. It is the exchange of fluid across “boundaries” which is of the greatest interest here and we first present the terminology and general description of *lobe dynamics* (see [17,25,28]).

Let $f : \mathbb{R}^2 \rightarrow \mathbb{R}^2$ be a differentiable, orientation preserving map, with f^k denoting the k th iterate of the map. In the context of this paper the map is the Poincaré map associated with the time-periodic system of ODEs. Consider fixed points p which are of saddle-type, that is, the Jacobian $Df(p)$ has one stable eigenvalue, $0 < \lambda_1 < 1$, and one unstable eigenvalue, $\lambda_2 > 1$. For incompressible flows the eigenvalues satisfy $\lambda_1 \cdot \lambda_2 = 1$. The stable manifold $W^s(p)$ is a 1D

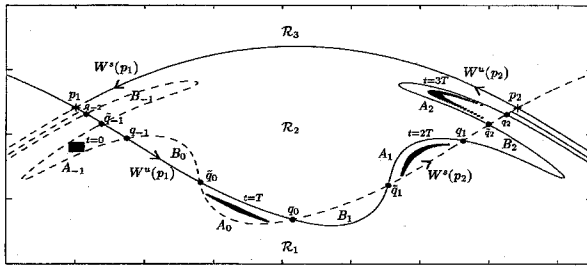


Fig. 3. Chaotic transport computed for a time-periodic flow modeling a meandering jet in [18]. The transverse intersections of $W^u(p_1)$ and $W^s(p_2)$ result in large fluxes across the boundary separating \mathcal{R}_1 and \mathcal{R}_2 , with turnstile lobes A_0 and B_0 . The transverse intersections between $W^s(p_1)$ and $W^u(p_2)$ are nearly negligible and there is little exchange of fluid between \mathcal{R}_2 and \mathcal{R}_3 .

curve consisting of all points q such that $f^k(q) \rightarrow p$ as $k \rightarrow \infty$. Similarly, the unstable manifold $W^u(p)$ is the set of all points asymptotic to p as $k \rightarrow -\infty$.

Suppose p_1 and p_2 are distinct hyperbolic fixed points of the map with the unstable manifold $W^u(p_1)$ intersecting transversely the stable manifold $W^s(p_2)$ (see Fig. 3). Points in the intersection $W^u(p_1) \cap W^s(p_2)$ are *heteroclinic points*, asymptotically approaching p_1 under backward iteration and asymptotic to p_2 under forward iteration. From the invariance of W^u and W^s and the fact that the flow is time-periodic, a single intersection point implies infinitely many intersections. Given an intersection point q , it is convenient to use $U[p_1, q]$ to denote the segment of $W^u(p_1)$ joining p_1 to q , and $S[p_2, q]$ to denote the segment of $W^s(p_2)$ joining p_2 to q . A point of intersection q is called a *primary intersection point (pip)* if the segments $U[p_1, q]$ and $S[p_2, q]$ intersect only at q . The map f being orientable ensures that if q is a pip, then $f^k(q)$ is a pip for all iterates k . A lobe is defined as the region bounded by segments of stable and unstable manifold joining an adjacent pair of pips. Lobes get mapped to lobes under the map f , and for incompressible flows, the area of the lobe remains constant under iterations of f . For the invariant manifolds $W^u(p_1)$ and $W^s(p_2)$ shown in Fig. 3 all of the lobes are generated by iterations of the two lobes labeled A_0 and B_0 . That is, $A_k = f^k(A_0)$ and $B_k = f^k(B_0)$ for any integer

k . More generally, if the intersections are transverse, there will be an even number of lobes which generate the entire infinite set of lobes under iterations of the map f .

Observe that the phase space in Fig. 3 has three distinct regions with qualitatively different motion. In the lower region \mathcal{R}_1 the flow is left to right (prograde) and trajectories are unbounded. Trajectories are also unbounded in the upper part of the phase space, denoted \mathcal{R}_3 , with the motion right to left (retrograde). Within the vortex region \mathcal{R}_2 the fluid circulates with a counterclockwise rotation. The invariant manifolds $W^u(p_1)$ and $W^s(p_2)$ intersect transversely and the strong intersections result in rather large lobes bounded by segments of stable and unstable manifolds. The structure of these lobes provides a geometric description of fluid exchange between the prograde region and the vortex region. Segments of the stable and unstable manifolds are used to partition the phase space into distinct regions. Choosing a pip q_0 defines a boundary between the two regions \mathcal{R}_1 and \mathcal{R}_2 by the union of the two segments $U[p_1, q_0]$ and $S[p_2, q_0]$. With this definition of a boundary, lobe A_0 lies inside region \mathcal{R}_1 , while A_1 lies inside \mathcal{R}_2 . Similarly, lobe B_0 lies inside \mathcal{R}_2 , whereas B_1 lies inside \mathcal{R}_1 . Fluid has been exchanged between regions \mathcal{R}_1 and \mathcal{R}_2 , and the lobes just preceding this exchange, A_0 and B_0 , are called the *turnstile lobes*. The area of lobe A_0 gives the amount of fluid passing from \mathcal{R}_1 to \mathcal{R}_2 in the course of one time period and dividing this area by the period of the Poincaré map gives an average flux across the boundary. This exchange of fluid between distinct regions of the phase space is also illustrated in Fig. 3 by following a patch of fluid particles through several iterations of the map. The parcels are initialized in lobe A_{-1} within region \mathcal{R}_1 and enter region \mathcal{R}_2 after two time periods, remaining inside the circulating region of the flow for several more time periods. At the same time fluid in lobe B_0 exits the vortex region in one time period and is transported downstream in the body of the jet. We note that in the upper part of the figure the manifolds $W^s(p_1)$ and $W^u(p_2)$ also intersect transversely but the transversality is considerably weaker and very little exchange takes place.

5. Transport in the time-periodic flow

In the following sections we present the results of the dynamical systems analysis using the data set with $(Re, \beta, n_0) = (10^4, 0.207, 4)$. The numerical solution is computed on a 64×64 spatial grid, with the solution saved at timesteps of $\Delta t = 0.25$ beginning with $t_0 = 300$. As described in Section 2, the meander propagates in the eastward direction with a nearly constant speed and the Lagrangian trajectories are computed in a reference frame moving along with the meander, greatly reducing the time dependence in the velocity field. For this set of parameters the time period associated with the meander propagation is $T_0 = 38.50$ corresponding to the propagation speed, $c = 0.1662$. The coordinates in the moving frame are (ξ, y, t) with $\xi = x - ct$, and the trajectories with respect to this translating frame are governed by the system of ODEs,

$$\begin{aligned} \frac{d\xi}{dt} &= u(\xi + ct, y, t) - c, \\ \frac{dy}{dt} &= v(\xi + ct, y, t). \end{aligned} \tag{6}$$

The flow is incompressible with the velocity field determined from the streamfunction $\psi(x, y, t)$. The spatial derivatives ψ_x , ψ_y and ψ_{xy} are computed at the grid points using the spectral representation of the streamfunction and interpolated to intermediate points using the local bicubic method described in Section 3.2. The velocity field is integrated using the fourth-order Runge–Kutta method with stepsize $h = 0.50$, requiring no interpolation in time. In the dynamical analysis the time of the initial slice in the data set is referred to as $t = 0$.

In this section the full data set is approximated with a periodic truncated data set with period T_1 determined by the dominant time dependence in the vector field as viewed in the moving frame. The data set is truncated at the slice preceding T_1 ; that is, the data set to be used for computing trajectories runs from $t = 0$ through $t = T_1 - \Delta t$. When the integration reaches $t = T_1$ the computation returns to the data set at $t = 0$. In this way the data set is forced to be periodic with period T_1 , exactly matching the PDE solution for one period, but deviating from the PDE solution for times

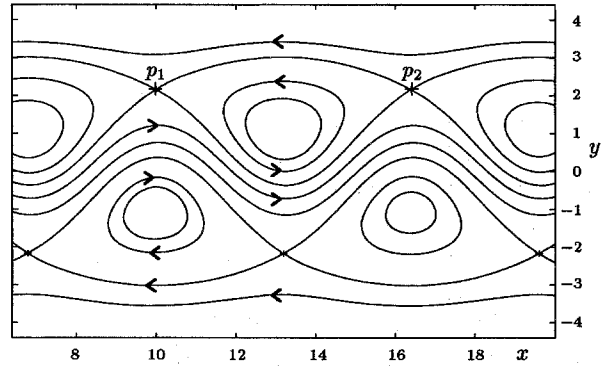


Fig. 4. Time-averaged streamfunction for $(Re, \beta, n_0) = (10^4, 0.207, 4)$. Our analysis identifies saddle-type fixed points in the Poincaré map which are close to the saddle points p_1 and p_2 , with transversely intersecting stable and unstable manifolds. Lobe dynamics pictured in Fig. 5 are computed just for the vortex region lying between p_1 and p_2 .

beyond one period. The Poincaré map for this periodic flow is defined in the usual way by using the period of the flow to define the time period of the map. Letting $\phi(t; \mathbf{x}_0, t_0)$ denote the solution to the initial value problem with $\mathbf{x}(t_0) = \mathbf{x}_0$, define the Poincaré map with $t_0 = 0$ as the reference slice,

$$\mathcal{P}(\mathbf{x}) = \phi(T_1; \mathbf{x}, 0), \tag{7}$$

mapping each point in phase space to the location of its trajectory at the end of one time period.

In this moving frame, the time-averaged vector field defines an integrable flow with two rows of cat's eyes (see Fig. 4). Each cat's eye is defined by a pair of heteroclinic orbits connecting an adjacent pair of saddle-type critical points (see p_1 and p_2 in Fig. 4). For the time-periodic flow we search for saddle-type fixed points to the Poincaré map existing in the vicinity of the saddle-type critical points for the time-averaged flow. If saddle fixed points exist for the map we generically expect that their stable and unstable manifolds will intersect transversely, creating a lobe structure as described in Section 4. The areas of the turnstile lobes associated with the intersecting manifolds quantify the exchange of fluid between different regimes over one time period of the flow, serving as an estimate for the fluxes in the full aperiodic flow.

5.1. Hyperbolic fixed points and invariant manifolds

The fixed point of the map $\mathcal{P} : \mathbb{R}^2 \rightarrow \mathbb{R}^2$ is determined by finding the zero of the function $G = \mathcal{P} - I$, where I is the identity map in \mathbb{R}^2 . Newton's method for finding zeroes will be successful if the initial guess is sufficiently close to the fixed point, and in that case, the convergence is very fast. However, the saddle-type fixed points in these maps have unstable eigenvalues on the order of 10^3 , and with these large stretching rates the Newton iteration quickly leaves the neighborhood of the initial point, even for very good initial guesses. As a rough estimate, if \bar{x} denotes the fixed point and λ^u the unstable eigenvalue at \bar{x} , we should expect x_n satisfying $|x_n - \bar{x}| \ll 1/\lambda^u$ to ensure that the next iteration moves much less than an $O(1)$ distance away from the current iteration. This is consistent with observations that the standard Newton method was often unsuccessful for initial guesses within as little as 10^{-3} of the fixed point.

In cases where we can make good initial guesses for the fixed points adding *backtracking* to the Newton method has been successful. In this method the next iteration is given by

$$x_{n+1} = x_n - \mu [DG(x_n)]^{-1} \cdot G(x_n), \quad (8)$$

where μ lies in the interval $0 < \mu \leq 1$ (see [21]). This chooses the next iteration to lie somewhere along the line segment joining the current iteration and the standard Newton iteration. If the standard Newton step ($\mu = 1$) is not closer to satisfying $G = 0$, the algorithm backtracks toward the current iteration ($\mu \rightarrow 0^+$) to find a new iteration which reduces $|G|$. By also restricting the distance between adjacent iterations the algorithm is able to make incremental improvements while staying in a small neighborhood of the initial guess, until the rapid convergence of the Newton method takes over.

The 1D invariant manifolds for the saddle-type fixed points can be approximated by iterating initial points clustered about the fixed point. When iterating forward, the points undergo strong stretching along the unstable direction and strong contraction in the stable direction, with the result that the points quickly align with the unstable manifold. Similarly, under back-

wards iteration the points lie near the stable manifold. A better initialization is to choose a linear segment of initial conditions which lie along the direction of the appropriate eigenvector for the fixed point. However, this simple approach can be rather ineffective for saddle points with large unstable eigenvalues. After several iterations of the map, the points will bunch up along some portions of the invariant curve while leaving other portions completely unresolved. Increasing the density of the initial cluster of points may improve the resolution but the effect is always very nonuniform over the length of the manifold and eventually becomes too inefficient, requiring excessively long computation times.

The algorithm used here for computing the unstable manifold begins by iterating a single point lying very near the fixed point in the direction of the unstable eigenvector. The segment defined by the initial point and its iteration is then iterated under the forward flow as many times as necessary to generate the unstable manifold to a desired length. Similarly, the stable manifold is approximated using the time-reversed flow to iterate points which initially lie along the stable eigenvector. Wherever the manifold is not sufficiently resolved after the k th iteration, additional points are inserted via linear interpolation of the unstable manifold at the $k - 1$ iteration. These additional points are mapped through a single iteration and merged with the existing curve of points. This approach assumes that after each iteration the curve is sufficiently resolved such that the interpolation provides an accurate approximation to the curve. The efficiency of this method lies in the fact that the map is iterated only for points which are likely to enhance the resolution of the curve. (This method is similar to the algorithm described in [14].) For the manifolds presented here the maximum distance between any two adjacent points on the invariant curve is 0.02.

5.2. Lobe dynamics and transport

The Poincaré map for the periodic truncated flow has two rows of hyperbolic fixed points just as the time-averaged flow in Fig. 4 has two rows of saddle-type critical points. We use this periodic flow to

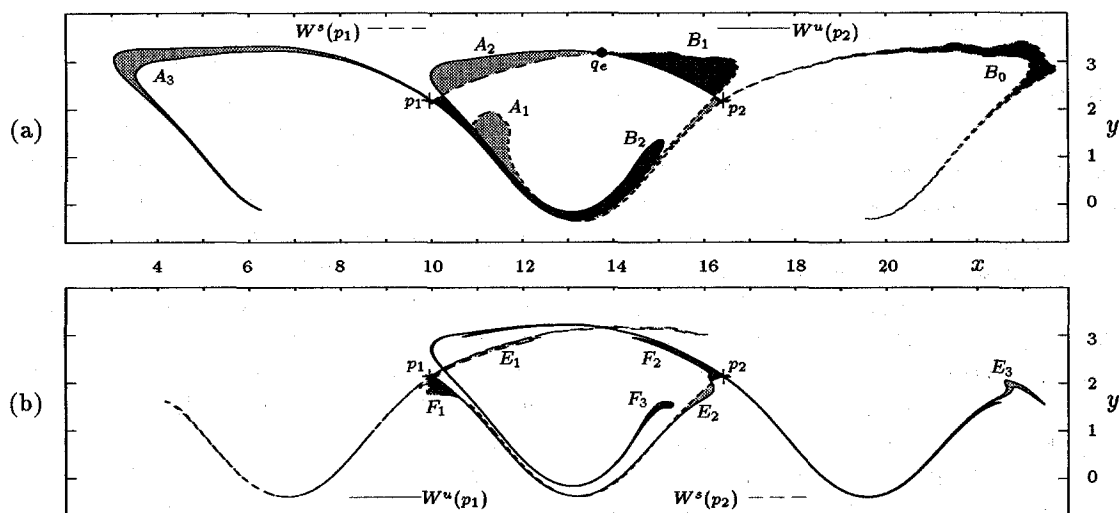


Fig. 5. Computed stable and unstable manifolds for $(Re, \beta, n_0) = (10^4, 0.207, 4)$ and the resulting lobes, using the periodic truncated flow. (a) Across the exterior boundary fluid leaves the recirculation region in moving from A_1 to A_2 and enters the recirculation when mapped from B_1 to B_2 . (b) The interior boundary has four distinct turnstile lobes but with considerably less area than the lobes in (a). Only the two largest lobes, E and F , are identified in (b).

estimate the Lagrangian transport between the three distinct regions of the flow, the eastward flowing (prograde) meandering jet, the vortex regions bounding the jet to the north and south, and the westward flowing (retrograde) regions outside the rows of vortices. Exchange of fluid between the recirculation regions and the retrograde regions is referred to as exchange across the *exterior* boundary, exchange between the recirculation regions and the body of the jet is referred to as exchange across the *interior* boundary. In all of the numerical solutions simulating meandering jets the most significant exchange of fluid takes place between the recirculation regions and the retrograde region outside of the jet. A more detailed analysis of the lobe dynamics and transport calculations for the periodic flow can be found in [22] where the PDE solution was computed for four different sets of parameter values using the higher resolution 128×128 spatial grid.

With the periodicity in x and the symmetry about $y = 0$, it is sufficient to study a single vortex structure and its corresponding pair of hyperbolic fixed points. The computations are done for a single vortex structure lying to the north of the jet axis so in all the pictures to be presented the exterior boundary is the upper

boundary and the interior boundary is to the south. The fixed point on the left is labeled p_1 and the fixed point on the right p_2 . Fluxes across the exterior boundary are characterized through the transverse intersection of the stable manifold $W^s(p_1)$ and the unstable manifold $W^u(p_2)$, while exchange across the interior boundary is through the transverse intersection of $W^u(p_1)$ and $W^s(p_2)$. The fluxes are found by computing the areas of the lobes associated with the principal intersections of stable and unstable manifolds. The principal intersection points are accurately estimated with the help of the computational package *Matlab*. Using the location of the pips, the manifolds can be separated into segments corresponding to distinct lobes and the lobe areas accurately estimated using an application of Green's Theorem. The area of a lobe existing between pips p and q is calculated by integrating the one form $x dy - y dx$ around the closed boundary of the lobe formed from the union $U[p, q] \cup S[p, q]$.

In each of the parameter cases investigated we found that the most significant exchange of fluid takes place across the exterior boundary of the jet between the vortex region and the retrograde region. Fig. 5 shows the invariant manifolds for the Poincaré map derived from the flow with $(Re, \beta, n_0) = (10^4, 0.207, 4)$ on

the 64×64 grid where the nondimensional time period of the map is $T_1 = 30.50$. In (a) the exterior boundary is defined by the union $S[p_1, q_e] \cup U[p_2, q_e]$ and there are two turnstile lobes, denoted A_1 and B_1 . The mapping $A_1 \xrightarrow{\mathcal{P}} A_2$ takes fluid from the vortex region to the retrograde region, and lobe $B_1 \xrightarrow{\mathcal{P}} B_2$ is fluid entering the vortex in forward time. The computed nondimensional lobe areas are 1.1366 for both sets of lobes, A and B , and these areas remain constant for all iterations of the lobes. Along the *interior* boundary (b) there are four turnstile lobes though the flux is considerably less than across the exterior boundary. The total area of the lobes entering the vortex from the jet is 0.2113, same as the amount of fluid leaving the vortex across the interior boundary.

6. Transport in the aperiodic flow

The lobe dynamics presented in Section 5.2 are for a periodic flow which approximates the aperiodic flow computed from the PDE. In this section we compute similar geometric structures for the full aperiodic velocity field covering four time periods of the Poincaré map, $0 \leq t \leq 122$. As a means of comparison with transport estimates from periodic flows we also repeat the lobe calculations in Section 5 for periodic flows defined on each of the four time intervals, $0 \leq t < 30.5$, $30.5 \leq t < 61.0$, $61.0 \leq t < 91.5$, and $91.5 \leq t < 122.0$.

For general time dependence in the 2D vector field it is convenient to consider the dynamical system as a flow on the *extended* phase space $\mathbb{R}^2 \times \mathbb{R}$. The equations in (6) are augmented in a trivial manner by adding a third differential equation for the time variable.

$$\begin{aligned}\dot{\xi} &= u(\xi + ct, y, t) - c, \\ \dot{y} &= v(\xi + ct, y, t), \\ \dot{t} &= 1.\end{aligned}\tag{9}$$

When the vector field is time-periodic the Poincaré map is a natural reduction to two dimensions. As viewed in this full 3D flow, a hyperbolic fixed point of the Poincaré map is a hyperbolic periodic trajectory, denoted $\gamma(t)$. The set of initial conditions which are

asymptotic (at an exponential rate) to $\gamma(t)$ in forward time define a 2D invariant set, the *stable* manifold, W_γ^s . The set of initial conditions which are asymptotic to $\gamma(t)$ in backward time define the 2D *unstable* manifold, W_γ^u . The 1D stable and unstable manifolds for the Poincaré map are just the intersection of these 2D manifolds with the time slice $t = t_0$. The intersection points for the map lie on heteroclinic trajectories, solution curves in the extended flow which are asymptotic to $\gamma(t)$ in both backwards and forwards time ($t \rightarrow \pm\infty$). Choosing a different cross-section in t changes the position of the lobes and intersection points, and therefore changes our definition of boundaries separating the different flow regimes, though the choice of reference time for defining the map does not affect either the interpretation of the lobe dynamics or the value of the time-averaged flux.

For the aperiodic flow we want to identify a distinguished hyperbolic trajectory which plays the same role in the Lagrangian mixing as the periodic trajectory $\gamma(t)$ for the time-periodic flow. However, in contrast to the periodic flow, we now have a strict limit on the length of time which we can follow trajectories and we can no longer rigorously define asymptotic structures such as stable and unstable manifolds. Rather, we will define this distinguished trajectory as the intersection of two invariant surfaces (invariant relative to the finite time interval) which are constructed in the same way as the stable and unstable manifolds for the periodic flow.

To understand the construction of the manifolds for the aperiodic flow, first consider how the manifolds are approximated for the time-periodic flow. The strong hyperbolicity in the neighborhood of the periodic orbit enables us to get reliable numerical approximations to the invariant manifolds. For initial points near the periodic trajectory the vector component in the stable direction sees a strong contraction in forward time and the solution should lie exponentially close to the unstable manifold in a very short time. At the same time, the distance from the fixed point will increase rapidly along the unstable eigendirection. Now consider initializing the periodic flow with a short line segment of initial conditions which lie along the unstable eigenvector of the fixed point but such that the fixed point is

interior to the interval (we say that the segment *straddles*¹ the hyperbolic trajectory). Integrating the flow forwards in time, the line segment now stretches in opposite directions, approximating both “halves” of the unstable manifold. At any fixed time slice the hyperbolic periodic trajectory remains straddled by the 1D section of the unstable manifold. In fact, such a straddling technique could be used to find a good approximation to the unstable manifold without first determining the precise periodic trajectory, as long as the initial line segment is close to the fixed point.

For the finite-time, aperiodic data sets we construct a 2D invariant manifold in the extended phase space by evolving forwards in time a short segment of initial conditions. For this “finite-time” unstable manifold, the initial line segment is chosen to *straddle* the hyperbolic region at $t = 0$ and aligned with the unstable eigendirection. The hyperbolic region is said to be straddled if the two ends of the curve stretch rapidly in opposite directions relative to an interior point of the segment. Similarly we construct a “finite-time” stable manifold, by evolving backwards in time a short segment of initial conditions chosen to straddle the appropriate hyperbolic region at $t = 122$ and aligned with the stable eigendirection.

The initialization for the unstable manifold uses the fixed point and eigenvector information from the time-map defined on the interval $0 \leq t \leq 30.5$. The evolution of the unstable manifold is shown by the solid curve in Fig. 6. The initial line segment chosen at $t = 0$ (Fig. 6(a)) is aligned with the unstable eigenvector and made to straddle the hyperbolic region denoted by p_2 . Under the forward flow (follow Figs. 6(a), (b), (c), etc.) the solid curve stretches rapidly in opposite directions, always straddling the region of hyperbolicity. Note that in Fig. 6 we have clipped half of the unstable manifold which forms the interior boundary between the jet core and the adjacent recirculation region.

The initialization for the stable manifold uses the fixed point and eigenvector information from the time-map defined on the interval $91.5 \leq t \leq 122.0$. The evolution of the stable manifold is shown by

the dashed curve in Fig. 6. The initial line segment chosen at $t = 122.0$ (Fig. 6(e)) is aligned with the stable eigenvector and made to straddle the hyperbolic region denoted by p_1 . Under the time-reversed flow (follow Figs. 6(e), (d), (c), etc.) the dashed curve stretches rapidly in opposite directions, always straddling the region of hyperbolicity. Again, in Fig. 6 we have clipped half of the stable manifold which forms a boundary for the neighboring recirculation region.

The computed manifolds are plotted in Fig. 6 at the time slices $t = mT_1$, for $m = 0, 1, \dots, 4$, where $T_1 = 30.5$ is the period used in the Poincaré map. The sections of invariant manifolds show an approximately recurrent behavior very similar in appearance to the iterated lobes for the Poincaré map as shown in Fig. 5. As with the invariant manifolds for the map we can also define lobes by the transverse intersection of the stable and unstable manifolds. However, for the aperiodic flow the manifolds are not easily computed to arbitrary lengths making it difficult to define very many lobes. For example, the unstable manifold is not known at $t = 0$ and is still not very long at $t = 30.5$. Similarly, the stable manifold is not well known at $t = 122.0$ and $t = 91.5$. Identifying more turnstile lobes or following additional iterations of the existing lobes requires saving the PDE solution on longer time intervals.

For the time interval used in this analysis we are able to follow the evolution of six lobes created by the intersection of these stable and unstable manifolds. In Fig. 6 the lobes are labeled $C-H$ and the iteration indices $0, \dots, 4$ correspond to the time slices, $t = 0$, $t = 30.5$, $t = 61.0$, $t = 91.5$ and $t = 122.0$, respectively. For comparison with the Poincaré map, lobes C , E and G correspond with the iterations of the A lobes and D , F and H are similar to the B lobes. For the aperiodic flow the exterior boundary may be changing in time, but nonetheless it is quite clear which regions of phase space are going from retrograde motion to vortex motion and which regions of fluid are leaving the vortex. That is, these finite-time stable and unstable manifolds clearly delineate regions of phase space having qualitatively different Lagrangian motion. For example, in going from $t = 30.5$ to $t = 61.0$ fluid in lobe E_1 passes out of the vortex into the retrograde

¹ We are borrowing here a term originally coined by Yorke and collaborators; see, for instance, [29].

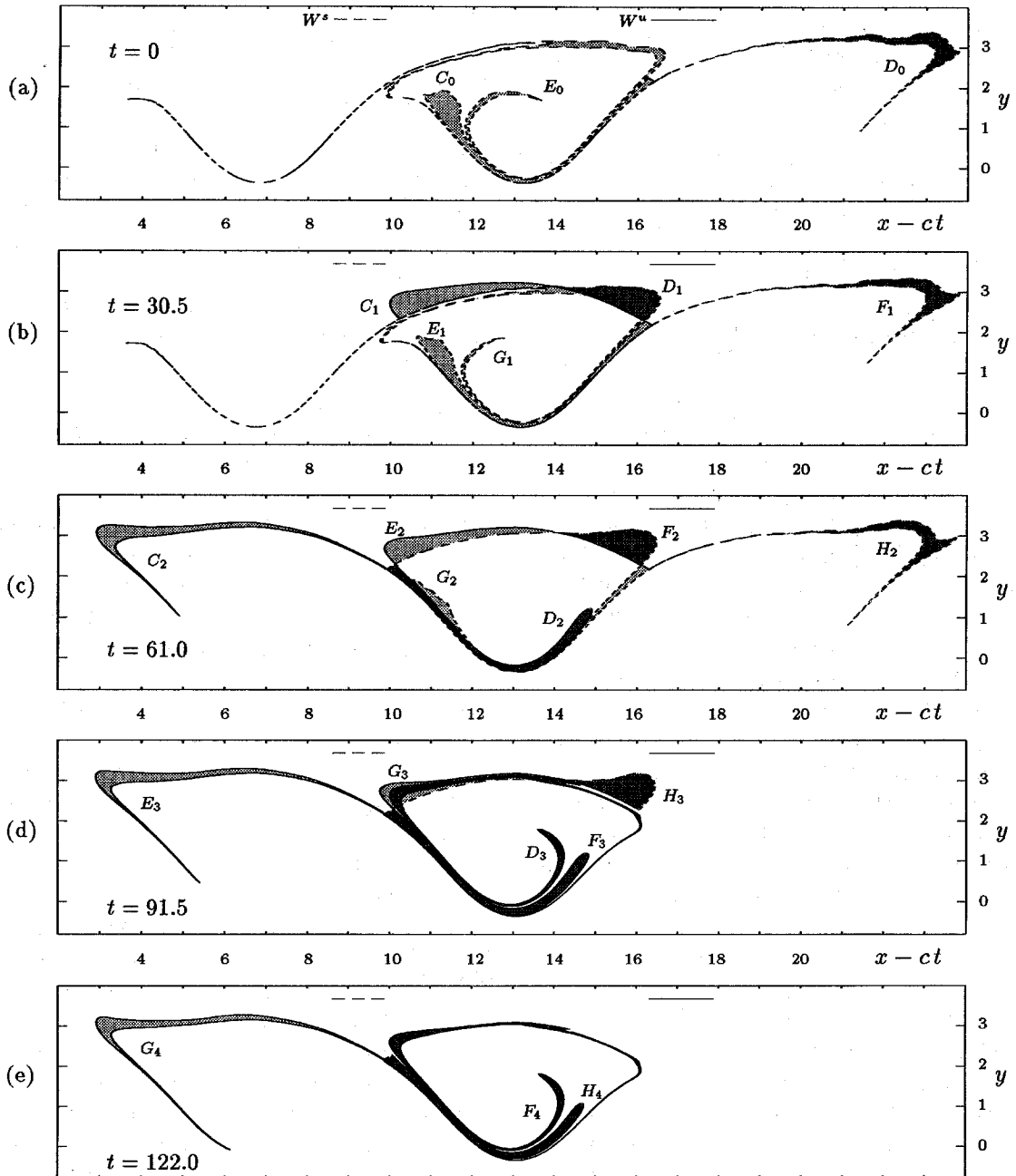


Fig. 6. Finite-time “stable” and “unstable” manifolds for the *aperiodic* flow. The cross-sections are plotted at multiples of the period $T_1 = 30.5$ for comparison with the lobes from the periodic flow in Fig. 5. We are able to identify six distinct lobes, C, \dots, H .

region (lobe E_2) and continues in retrograde motion for at least another time period (lobe E_3). At the same time fluid in lobe D_1 will exit from retrograde motion during the next time period, entering the vortex

(lobe D_2). Although the definition of our boundary may change from slice to slice, we can still identify turnstile lobes and quantify a time-averaged flux between the two regions. The lobe areas are summarized

Table 1
Estimated transport for the *aperiodic* flow covering $0 \leq t \leq 122$

Lobe	Exchange	Period	Area	\mathcal{P}
<i>C</i>	<i>vort</i> → <i>retr</i>	0.0–30.5	1.112	1.137
<i>D</i>	<i>retr</i> → <i>vort</i>	30.5–61.0	0.982	1.037
<i>E</i>	<i>vort</i> → <i>retr</i>	30.5–61.0	1.055	1.037
<i>F</i>	<i>retr</i> → <i>vort</i>	61.0–91.5	0.955	0.992
<i>G</i>	<i>vort</i> → <i>retr</i>	61.0–91.5	1.004	0.992
<i>H</i>	<i>retr</i> → <i>vort</i>	91.5–122.0	0.889	0.931

The labels *vort* and *retr* refer to the vortex and retrograde regions, respectively. “Period” indicates the time interval in which the exchange takes place. The final column \mathcal{P} is the lobe area from the Poincaré map for the corresponding time period.

in Table 1 showing that the flux is slowly decreasing with time. For comparison, the Poincaré map was computed using a periodic truncation on each of the four time intervals. The flux estimates computed from the maps for these truncated periodic flows are included in Table 1 along with the time-dependent fluxes computed from the full aperiodic data set.

7. Robustness of lobe calculations

In this section we remark on the robustness of the lobe calculations. There are a number of numerical issues affecting the calculation of particle trajectories; the temporal resolution of the data base, the time stepping used in integrating the vector field, the spatial interpolation, and the numerical differentiation. To test the sensitivity of these transport calculations to changes in numerical parameters a number of experiments were conducted using the data set with $(Re, \beta, n_0) = (10^4, 0.207, 4)$. As a benchmark we use the results computed in Section 5 for the truncated periodic flow using the numerical velocity field from the interval $0 \leq t < 30.5$. Recall the numerical parameters for the calculations in Section 5; the resolution of the data base is $\Delta t = 0.25$, the stepsize for the fourth-order Runge–Kutta is $h = 0.50$, interpolation in x – y space uses the local bicubic scheme, and all spatial derivatives are computed in Fourier space providing full spectral accuracy at the nodes. Comparisons are made with respect to the location of the fixed point p_1 and the computed areas for three iterations of the *A* lobes along the exterior boundary as

Table 2
Summary of experiments with variations in numerical parameters

Δt	Interpolation	Derivatives	Change in p_1	Area of <i>A</i> lobes
0.25	<i>bicubic</i>	<i>spect</i>	0.0	1.13658–1.13663
0.05	<i>bicubic</i>	<i>spect</i>	0.0328	1.13639–1.13645
0.25	LP (6×6)	<i>spect</i>	0.0018	1.13669–1.13824
0.25	<i>bicubic</i>	cdiff	0.0070	1.13150–1.13159

The resolution in the numerical vector field is denoted Δt and the timestep used in the ODE solver is $h = 2 \cdot \Delta t$. Spatial interpolation uses either the local bicubic interpolation described in Section 3 or the Lagrange polynomial on a local 6×6 grid. Spatial derivatives are computed in Fourier space or by centered differences. The column “change in p_1 ” records the location of fixed point p_1 relative to the results in the first row. The last column lists the range of areas computed for the three iterations of the *A* lobes shown in Fig. 5.

shown in Fig. 5. The results from these experiments are summarized in Table 2.

The first experiment compares results for different temporal resolutions in the numerical vector field. The analysis was performed on a data set with the solution written at intervals of $\Delta t = 0.05$, the smallest interval available from the PDE solver. The ODEs were integrated at a timestep $h = 0.10$ requiring no temporal interpolation. The fixed point p_1 shifted by a distance 0.006, insignificant relative to the distance between adjacent hyperbolic points, and perhaps more importantly, the area of lobe A_2 changed from 1.1366 to 1.1364, less than 0.02%. We also note that results obtained from the coarser data set ($\Delta t = 0.25$) using $h = 0.05$ and different orders of temporal interpolation showed negligible difference from the benchmark results obtained using $h = 0.50$, also an indication that the data set is adequately resolved in time.

The second experiment analyzed the data set using the Lagrangian polynomial interpolation on a local 6×6 grid to compare with the lower order, though smoother, bicubic interpolation. The average area of the *A* lobes is within 0.2% of the area computed using bicubic interpolation though, as expected, there is greater variation in the areas of the lobes from iteration to iteration since the interpolations are done independently, resulting in some loss of Hamiltonian structure. Over three iterations of the *A* lobes the variation in area is 0.00155, about 0.14% of the total area.

By comparison, the areas of the same set of A lobes computed using bicubic interpolation never varied by more than 0.00009, less than 0.01% of the total area. Even though the variation in area using Lagrangian interpolation is more than an order of magnitude greater than with the bicubic interpolation, the variation appears to be insignificant in this case.

The final experiment performed the lobe analysis using centered differences to compute the spatial derivatives, ψ_x , ψ_y , and ψ_{xy} . The advantage for the incompressible flows studied here is that the necessary derivatives can be computed efficiently from just a single scalar function. Of all the experiments, this change had the largest impact on the computed transport with the areas of the A lobes differing from the benchmark by approximately 0.4%, still a relatively insignificant difference.

The insensitivity in the lobe calculations with respect to variations in the numerical parameters makes this an attractive tool for studying the dynamics of numerically generated flows. The robustness of the calculations may just be due to the structural stability of hyperbolicity in dynamical systems. The dynamical systems analysis for characterizing transport is based on the existence of certain geometric features associated with hyperbolic regions of the flow. Changes in the numerical parameters are equivalent to small perturbations in the vector field which do not significantly affect the hyperbolic structure of the flow, resulting in small differences in the computed transport dynamics.

8. Discussion

The main result in this paper is the implementation of dynamical systems techniques for identifying lobe dynamics within 2D vector fields that are numerically generated solutions to the fully nonlinear governing PDEs. The computed lobes, defined by intersections of stable and unstable manifolds, effectively characterize and quantify the exchange of fluid between adjacent flow regimes within the phase space. We emphasize that the objective in this paper is to characterize the local fluxes between adjacent flow regimes, existing on some finite-time interval, rather than the long-time

global transport associated with fluxes across many boundaries within the flow.

The lobes are first constructed for the Poincaré map associated with a periodic flow that approximates the aperiodic vector field. Then, for the full aperiodic velocity field, “stable” and “unstable” manifolds are constructed from trajectories which emanate from regions of strong hyperbolicity, just as the invariant manifolds of the fixed points in the Poincaré map are approximated by trajectories initialized near the hyperbolic periodic orbit. These invariant manifolds intersect transversely and their cross-sections, defined by fixing a time slice, show lobe structures very similar to the lobes for the time-periodic flow. The fact that the geometry of the lobes has a strong time-recurrence, as shown in Fig. 6, is a reflection of the nearly periodic time dependence of the underlying flow. That this time period of recurrence agrees so well with the dominant time period T_1 used in defining the periodic flow indicates that T_1 is the correct time scale for describing the exchange of fluid between regions of retrograde motion and regions where the fluid is circulating.

For the data set analyzed here it is possible to generate several iterations of lobes for the aperiodic flow because the crucial hyperbolic regions persist for times much longer than the time scale T_1 associated with the local flux of fluid across the boundaries defining the recirculation region. Our ability to characterize the lobes over a relatively long-time interval is again a reflection of the nearly periodic time dependence in the data set.

Near-integrable flows which are almost periodic in time may lend themselves to rigorous asymptotic results regarding existence of stable and unstable manifolds as well as finite-time analytical transport estimates such as established for near-integrable, time-periodic flows in [23]. Moreover, lobe dynamics have been rigorously established for planar Hamiltonian systems with general time dependence by exploiting the singular perturbation structure of adiabatic systems [15]. In the analysis presented here however, we are interested in identifying the geometric structure of flows given as numerical solutions to the governing equations, situations in which the dynamical system is not necessarily near-integrable and the integration

is not easily extended to longer and longer time intervals. In the meandering jet simulations investigated here it is clear that the almost periodic time dependence plays an important role in enabling us to find meaningful structures for describing fluid exchange in the flow.

Quantifying fluxes in the flow requires that we define boundaries between different flow regimes using segments of the computed manifolds. For the time-periodic case this choice of boundary is well understood and provides a *fixed* partition of the phase space (see Section 4). For flows with general time dependence a strategy is needed for defining the boundary at different time slices and the partition of phase space will no longer be fixed for all times. The strong periodic component in the velocity field for the meandering jet made it quite natural to slice the 2D manifolds at time intervals equal to the dominant time period ($T_1 = 30.5$). At these intervals the boundaries appear nearly fixed and very similar to the boundaries for the periodic approximation.

The dynamical systems analysis for the aperiodic flow, summarized in Table 1, indicates that the fluxes across the recirculation boundary are decreasing with time, whereas for the periodic approximation in Section 5 the flux necessarily remains constant for all time. This decrease in the exchange of fluid is to be expected since the viscosity is dissipating energy in the higher modes. Perhaps a more interesting observation is that the flux estimates for the aperiodic flow show more fluid leaving the vortex region than entering during each time cycle (compare lobes *D* and *E*, and lobes *F* and *G* in Table 1). This can be explained by the fact that the entire vortex structure is shrinking as time evolves, again due to the dissipation of energy, and there is necessarily a net flux out of the recirculation region. On the other hand, the vortex region in the periodic flow, as defined by segments of the stable and unstable manifolds, must necessarily remain constant and this effect of the periodic truncation is reflected in a slightly larger flux of fluid entering the vortex.

In summary, this numerical simulation of a meandering jet has served to motivate the development of strategies and software tools for using lobe dynamics

to characterize fluxes in numerical simulations of 2D geophysical flows, where the time dependence is not necessarily periodic. We find that the computed lobe structures and flux calculations are quite robust with respect to variations in the numerical schemes. The particular velocity field presented here is a mild departure from periodicity and, as a result, the interpretation of the lobe dynamics is not significantly more difficult than the time-periodic case. A natural progression from here would be to consider flows with considerably stronger aperiodic time dependence but such that the crucial hyperbolic structures still persist for long times relative to the dominant time period of the flow. The persistence of the hyperbolic structures may still enable one to identify sufficiently long finite-time stable and unstable manifolds while the stronger aperiodicity should make the analysis of the lobe dynamics significantly more difficult and theoretically more interesting.

Acknowledgements

We gratefully acknowledge support from the Office of Naval Research, contract N00014-92-J-1481 for PDM and CKRTJ, N00014-89-J-1182 for LJP, and N00014-93-1-1369 for AMR. AMR also acknowledges the support of the National Science Foundation, grant OCE-9503014.

References

- [1] S. Balachandar and M.R. Maxey, Methods for evaluating fluid velocities in spectral simulations of turbulence, *J. Comput. Phys.* 83 (1) (1989) 96–125.
- [2] S. Balasuriya, C.K.R.T. Jones and B. Sandstede, Viscous perturbations of vorticity conserving flows and separatrix splitting, preprint.
- [3] D. Barkley, G.E. Karniadakis, I.G. Kevrekidis, Z. Shen and A.J. Smits, Chaotic advection in a complex annular geometry, *Phys. Fluids A* 3 (1991) 1063–1067.
- [4] D. Biegie, A. Leonard and S. Wiggins, Chaotic transport in the homoclinic and heteroclinic tangle regions of quasiperiodically forced two-dimensional dynamical systems, *Nonlinearity* 4 (1991) 775–819.
- [5] A. Bower, A simple kinematic mechanism for mixing fluid parcels across a meandering jet, *J. Phys. Oceanography* 21 (1) (1991) 173–180.

- [6] A. Bower and T. Rossby, Evidence of cross-frontal exchange processes in the gulf stream based on isopycnal rafofs float data, *J. Phys. Oceanography* 19 (9) (1989) 1177–1190.
- [7] M.G. Brown and R.M. Samelson, Particle motion in vorticity-conserving, two-dimensional incompressible flows, *Phys. Fluids* 6 (9) (1994) 2875–2876.
- [8] R. Camassa and S. Wiggins, Chaotic advection in Rayleigh–Bénard flow, *Phys. Rev. A* 43 (2) (1991) 774–797.
- [9] D. del Castillo-Negrete and P.J. Morrison, Chaotic transport of Rossby waves in shear flow, *Phys. Fluids A* 5 (4) (1993) 948–965.
- [10] J. Duan and S. Wiggins, Fluid exchange across a meandering jet with quasiperiodic variability, *J. Phys. Oceanography* 26 (1996) 1176–1188.
- [11] J. Duan and S. Wiggins, Lagrangian transport and chaos in the near wake of a cylinder in the time-periodic regime: A numerical implementation of lobe dynamics, preprint.
- [12] S. Dutkiewicz, A. Griffa and D.B. Olson, Particle diffusion in a meandering jet, *J. Geophys. Res.* 98 (1993) 16487–16500.
- [13] G. Flierl, P. Malanotte-Rizzoli and N. Zabusky, Nonlinear waves and coherent vortex structures in barotropic β -plane jets, *J. Phys. Oceanography* 17 (9) (1987) 1408–1438.
- [14] D. Hobson, An efficient method for computing invariant manifolds of planar maps, *J. Comput. Phys.* 104 (1) (1993) 14–22.
- [15] T. Kaper and S. Wiggins, Lobe area in adiabatic Hamiltonian systems, *Physica D* 51 (1) (1991) 205–212.
- [16] M.S. Lozier, L.J. Pratt, A.M. Rogerson and P.D. Miller, Exchange geometry revealed by float trajectories in the Gulf Stream, *J. Phys. Oceanography* (1997), to appear.
- [17] R.S. MacKay, J.D. Meiss and I.C. Percival, Transport in Hamiltonian systems, *Physica D* 13 (1984) 55–81.
- [18] P. Miller, C.K.R.T. Jones, G. Haller and L. Pratt, Chaotic mixing across oceanic jets, in: *Chaotic, Fractal and Nonlinear Signal Processing*, ed. R. Katz, AIP Conf. Proc., Vol. 375 (AIP Press, New York, 1996) pp. 591–604.
- [19] J.M. Ottino, *The Kinematics of Mixing: Stretching, Chaos, and Transport* (Cambridge University Press, Cambridge, 1989).
- [20] L.J. Pratt, M.S. Lozier and N. Beliakova, Parcel trajectories in quasigeostrophic jets: Neutral modes, *J. Phys. Oceanography* 25 (6) (1995) 1451–1466.
- [21] W.H. Press, S.A. Teukolsky, W.T. Vetterling and B.P. Flannery, *Numerical Recipes in C: The Art of Scientific Computing* (Cambridge University Press, Cambridge, 1992).
- [22] A.M. Rogerson, P.D. Miller, L.J. Pratt, C.K.R.T. Jones and J. Biello, Chaotic mixing in a barotropic meandering jet, preprint.
- [23] V. Rom-Kedar, Homoclinic tangles – Classification and applications, *Nonlinearity* 7 (1994) 441–473.
- [24] V. Rom-Kedar, A. Leonard and S. Wiggins, An analytical study of transport, mixing and chaos in an unsteady vortical flow, *J. Fluid Mech.* 214 (1990) 347–394.
- [25] V. Rom-Kedar and S. Wiggins, Transport in two-dimensional maps, *Arch. Rat. Mech. Anal.* 109 (1990) 239–298.
- [26] R.M. Samelson, Fluid exchange across a meandering jet, *J. Phys. Oceanography* 22 (4) (1992) 431–440.
- [27] K. Shariff, T.H. Pulliam and J.M. Ottino, A dynamical systems analysis of kinematics in the time-periodic wake of a circular cylinder, in: *Vortex Dynamics and Vortex Methods*, eds. C. Anderson and C. Greengard, Lectures in Mathematics (American Mathematical Society, Providence, RI, 1992) pp. 613–646.
- [28] S. Wiggins, *Chaotic Transport in Dynamical Systems*, Interdisciplinary Applied Mathematics, Vol. 2 (Springer, Berlin, 1992).
- [29] H. Nusse and J. Yorke, *Dynamics: Numerical Explorations* (Springer, Berlin, 1994).